Nano Today 46 (2022) 101557

Contents lists available at ScienceDirect

Nano Today

journal homepage: www.elsevier.com/locate/nanotoday

Fully implantable batteryless soft platforms with printed nanomaterial-based arterial stiffness sensors for wireless continuous monitoring of restenosis in real time

Robert Herbert[a,b], Moataz Elsisy[c], Bruno Rigo[b,d], Hyo-Ryoung Lim[e], Hyeonseok Kim[a,b], Chanyeong Choi[a,b], Seungil Kim[f,g], Sang-Ho Ye[f,g], William R. Wagner[f,g,h], Youngjae Chun[c,f,h,*], Woon-Hong Yeo[a,b,i,j,**]

[a] George W. Woodruff School of Mechanical Engineering, Georgia Institute of Technology, Atlanta, GA 30332, USA
[b] IEN Center for Human-Centric Interfaces and Engineering at the Institute for Electronics and Nanotechnology, Georgia Institute of Technology, Atlanta, GA 30332, USA
[c] Department of Industrial Engineering, Swanson School of Engineering, University of Pittsburgh, Pittsburgh, PA 15260, USA
[d] School of Electrical and Computer Engineering, Georgia Institute of Technology, Atlanta, GA 30332, USA
[e] Major of Human Biocovergence, Division of Smart Healthcare, College of Information Technology and Convergence, Pukyong National University, Busan 48513, Republic of Korea
[f] McGowan Institute for Regenerative Medicine, University of Pittsburgh, Pittsburgh, PA 15260, USA
[g] Departments of Surgery, University of Pittsburgh, Pittsburgh, PA 15260, USA
[h] Department of Bioengineering, University of Pittsburgh, Pittsburgh, PA 15261, USA
[i] Wallace H. Coulter Department of Biomedical Engineering, Parker H. Petit Institute for Bioengineering and Biosciences, Georgia Institute of Technology, Atlanta, GA 30332, USA
[j] Institute for Materials, Neural Engineering Center, Institute for Robotics and Intelligent Machines, Georgia Institute of Technology, Atlanta, GA 30332, USA

ARTICLE INFO

Article history:
Received 1 February 2022
Received in revised form 20 May 2022
Accepted 10 July 2022
Available online 18 July 2022

Keywords:
Wireless implantable soft platform
Strain sensor
Printed nanomaterials
Restenosis
Vascular electronics

ABSTRACT

Atherosclerosis is a common cause of coronary artery disease and a significant factor in broader cardiovascular diseases, the leading cause of death. While implantation of a stent is a prevalent treatment of coronary artery disease, a frequent complication is restenosis, where the stented artery narrows and stiffens. Although early detection of restenosis can be achieved by continuous monitoring, no available device offers such capability without surgeries. Here, we report a fully implantable soft electronic system without batteries and circuits, which still enables continuous wireless monitoring of restenosis in real-time with a set of nanomembrane strain sensors in an electronic stent. The low-profile system requires minimal invasive implantation to deploy the sensors into a blood vessel through catheterization. The entirely printed, nanomaterial-based set of soft membrane strain sensors utilizes a sliding mechanism to offer enhanced sensitivity and detection of low strain while unobtrusively integrating with an inductive stent for passive wireless sensing. The performance of the soft sensor platform is demonstrated by wireless monitoring of restenosis in an artery model and an ex-vivo study in a coronary artery of ovine hearts. The capacitive sensor-based artery implantation system offers unique advantages in wireless, real-time monitoring of stent treatments and arterial health for cardiovascular disease.

Introduction

Atherosclerosis, where arteries narrow as artery walls thicken and stiffen, is a leading cause of cardiovascular diseases [1,2]. In total, cardiovascular diseases are the most common cause of death and account for 31% of deaths [3]. Atherosclerosis can lead to a variety of conditions, including myocardial infarctions, angina, strokes, aneurysms, and gangrene, among others [1]. A common treatment of atherosclerosis is angioplasty and stenting, where the

* Corresponding author at: Department of Industrial Engineering, Swanson School of Engineering, University of Pittsburgh, Pittsburgh, PA 15260, USA.
** Corresponding author at: George W. Woodruff School of Mechanical Engineering and IEN Center for Human-Centric Interfaces and Engineering, Georgia Institute of Technology, Atlanta, GA 30332, USA.
E-mail addresses: yjchun@pitt.edu (Y. Chun), whyeo@gatech.edu (W.-H. Yeo).

https://doi.org/10.1016/j.nantod.2022.101557
1748-0132/

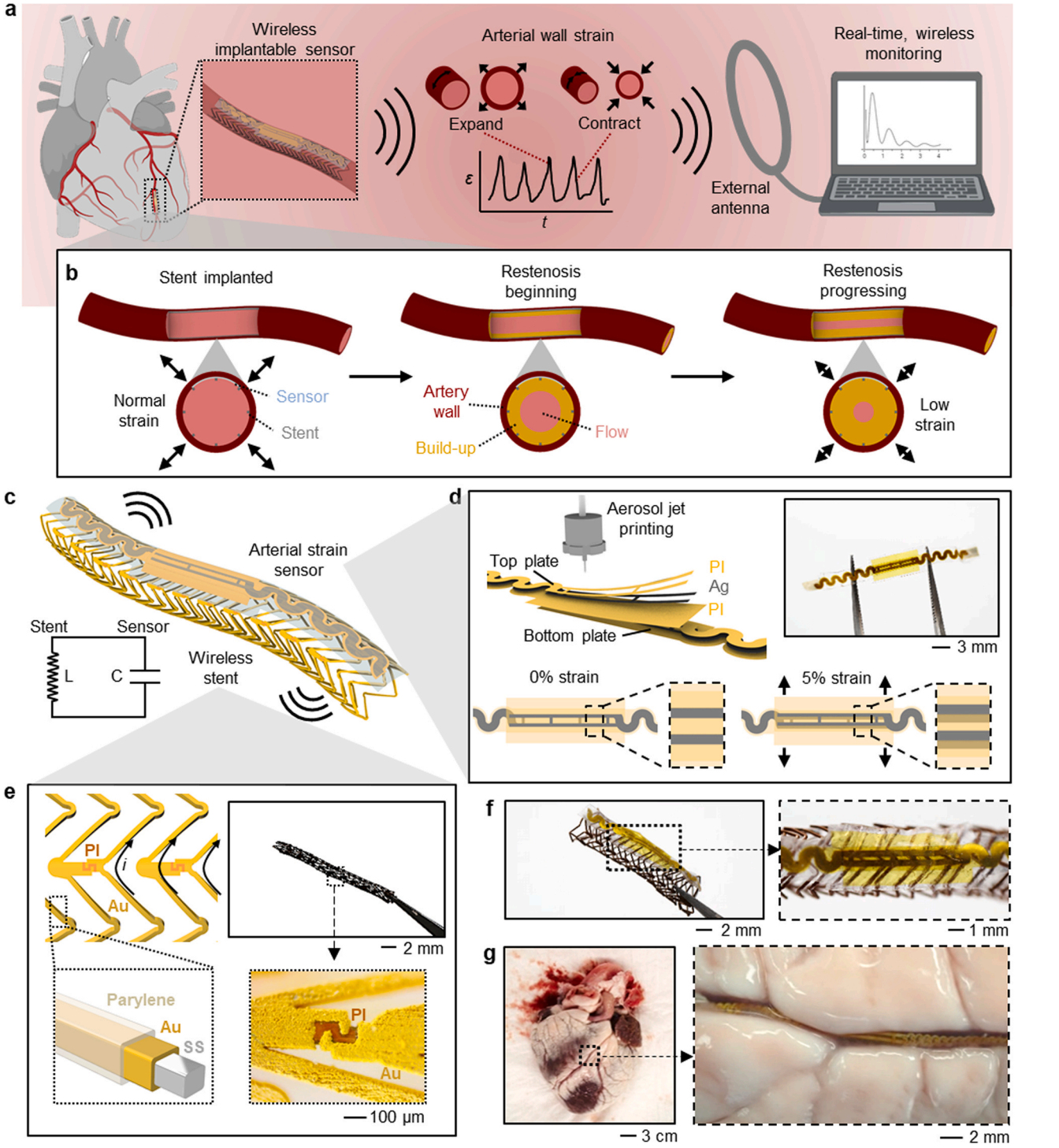

Fig. 1. Design of a fully implantable batteryless platform with membrane arterial stiffness sensors for wireless restenosis monitoring. (a) Illustration of an implanted wireless sensor for monitoring of arterial wall strain and restenosis detection. (b) Schematic of a stented artery during restenosis progression and the resulting change of arterial wall strain. (c) Illustration of the implantable device and equivalent electrical circuit comprised of capacitive strain sensor and inductive stent. (d) Illustration of aerosol jet printed, nanomaterial-based strain sensor showing layers of PI and AgNP. The top and bottom plates slide relative to each other to enable capacitive sensing of strain. The assembled sensor is imaged on tweezers. (e) Design of multi-material, wireless stent using Au loops and PI connectors to enable a solenoid-like flow of current. Loops consist of SS, Au, and parylene. The wireless stent is imaged on tweezers with an enlarged view of the PI connector. (f) Photo of a sensor-integrated stent with an enlarged view of the arterial strain sensor. (g) Photo of ovine heart with an implanted sensor with an enlarged view of the coronary artery.

narrowed artery is widened with a balloon catheter and then held open with a stent [4,5]. Although several million stents are implanted per year, a frequent complication of stenting is restenosis, where the treated artery narrows and stiffens again [6–9]. Restenosis is often defined as a lumen reduction of at least 50–70% with varying degrees of severity [10–12]. Restenosis progresses gradually and often causes no symptoms until the blockage becomes severe. While recent advances in drug-eluting stents have reduced restenosis rates to less than 10%, affordability and complication concerns exist for drug-eluting stents [6,8,13–15]. Thus, bare metal stents are still often used and have shown restenosis in 17–41% of treatments [7,8]. Notably, restenosis correlates with morbidity and a study has

previously indicated restenosis as a predictor of 4 year mortality [12,16]. Moreover, restenosis may be a risk factor of stent thrombosis, a rarer condition where an acute occlusion occurs of the stented artery [17]. While stent thrombosis occurs in approximately 1% of patients, it shows a mortality rate up to 45% [18,19]. Despite the high prevalence of restenosis, monitoring methods are limited to imaging techniques or catheterization, such as angiography, intravascular ultrasound, optical coherence tomography, and catheter-based measurements [12]. Follow-ups occur at varying intervals of time and, as a result, the progression of restenosis is incompletely monitored. Continuous monitoring would enable early detection and prevention of complications, especially since it has been shown that restenosis rates vary by patient, stent properties, and type of intervention [12,20].

Continuous, non-invasive monitoring of restenosis enabled by implantable electronics would allow early detection and management of patient health and provide a better understanding of stent designs to minimize restenosis. However, the development of implantable vascular electronics has been restricted due to stringent requirements associated with implantation and operation within soft, narrow arteries. Requirements include a miniaturized, low-profile structure to minimize the impact on blood flow, soft, flexible mechanics to interface with compliant arterial walls, and wireless sensing. Recent advances in soft, wireless electronics offer solutions for the design of implantable vascular sensors [21–29]. Multiple prior works have developed implantable vascular sensors for monitoring blood pressure, and a few have incorporated monitoring of blood flow [26,28,30–32]. These works have developed both stent-based sensors and sensors wrapped around the outside of an artery. While some stent-based devices apply a single pressure sensor with a target of monitoring occlusion, it cannot measure the fractional flow reserve (FFR) for restenosis or arterial distensibility [25,28]. FFR is a widely used measurement to determine the significance of the blockage and is measured by recording pressure both upstream and downstream of a restenosis [12,33]. One work employed two pressure sensors to measure FFR, but relies on x-ray imaging to read the sensor [32].

Alternatively to blood pressure monitoring, measuring arterial stiffness or distensibility offers a more direct means to quantify restenosis. As restenosis progresses, artery walls thicken and stiffen, decreasing arterial strain and distensibility. In a similar concept, prior works have investigated sensors to detect the expansion and contraction of arterial walls during blood flow [25,34–36]. These prior works have developed wireless pressure sensors to be wrapped around the artery to detect arterial occlusion [25,35]. Additionally, strain sensors, including a capacitive sensor and photonic sensor, have been studied for wrapping around an artery to measure response to blood pressure [34,36]. While these wrapped sensors demonstrate detection of an occlusion, implantation would be significantly more invasive than conventional catheterization procedures. Moreover, the prior wireless sensors do not demonstrate the ability to quantify restenosis or arterial stiffness and, thus, an implantable device is lacking [25,35]. Beyond restenosis, an arterial stiffness sensor would offer a broad impact on vascular sensing since arterial stiffness is a significant biomarker of cardiovascular disease and mortality [37–40]. Studies have demonstrated arterial stiffening as a warning sign of cardiovascular morbidity and mortality and is an independent predictor of cardiovascular diseases, including hypertension, atherosclerosis, coronary artery disease, strokes, and heart failures [37–40]. Arterial stiffening is also associated with a heightened risk of organ damage, including to the kidneys and brain, due to the effect on blood flow and pressure [37]. Thus, an arterial stiffness sensor could be readily extended to broader applications, such as continuously monitoring local arterial stiffness to understand the role of arterial stiffness further and as a preventative measure of cardiovascular diseases [41].

This article reports wireless soft electronics comprised of a capacitive strain sensor and an electronic stent to monitor arterial stiffness changes stemming from restenosis. The stent-based device is deployable by conventional balloon catheters for minimally invasive implantation and offers unobtrusive sensing of arterial wall strain changes during blood flow. The aerosol jet printed, nanomaterial-based soft strain sensor employs a sliding mechanism that is investigated and optimized to enhance sensitivity compared to existing soft, capacitive strain sensors. The highly flexible, nanomembrane strain sensor is integrated onto a multi-material, inductive antenna stent to enable wireless sensing via inductive coupling. The wireless vascular device is demonstrated in a biomimetic coronary artery model to detect restenosis progression. An ex-vivo study with ovine hearts demonstrates restenosis sensing in narrow coronary arteries.

Results and discussion

Design of a fully implantable batteryless platform with arterial stiffness sensors for wireless restenosis monitoring

A wireless implantable sensor system is developed to monitor the change in arterial stiffness stemming from restenosis, which measures arterial wall strain. Fig. 1a illustrates the overview of the monitoring system and arterial strain changes during blood flow. The implantable sensor, consisting of a soft strain sensor and electronic stent, is inductively coupled with an external antenna to record real-time changes in arterial wall strain as an artery expands and contracts. The stent-based device is implanted within an artery via a balloon catheter, identical to the current treatment of atherosclerosis of angioplasty and stenting. The monitored arterial stiffness changes with restenosis progression, as illustrated in Fig. 1b. The gradual build-up within the artery thickens and stiffens the artery wall, resulting in lower strain changes and higher stiffness. The change from normal strain to low strain is quantified to assess the severity of restenosis in the artery. The implantable device is comprised of a capacitive strain sensor laminated on an inductive stent, which forms an LC circuit with a resonant frequency dependent on strain (Fig. 1c). The soft strain sensor is orientated on the outer surface of the stent to detect circumferential strain in the artery. The integrated stent and sensor are operated via inductive coupling to wirelessly monitor changes in resonant frequency. The soft, arterial strain sensor is aerosol jet printed with silver nanoparticles (AgNP) and polyimide (PI) (Fig. 1d). Aerosol jet printing was selected as it is compatible with a wide range of ink viscosities (1 – 2500 cP). It is a digital, maskless form of printing, which allows for rapid prototyping and customization of printed devices. Moreover, this method allows for high-resolution printing of both conductive nanoparticle inks and polymer inks with thicknesses of a few microns, which is beneficial to form a low-profile, multi-layered sensor. Comparatively, screen printing offers lower resolution with thicker depositions while requiring fabrication of patterned masks [42–44]. Another form of digital printing is inkjet printing, but inkjet printers operate with a more narrow viscosity range incompatible with printing of higher viscosity polyimide [42–45]. A top and bottom plate are printed separately prior to transfer and assembly in elastomer encapsulation to form a parallel-plate capacitor (details in Methods and Fig. A.1). Elastomer encapsulations were made of poly(styrene-isoprene-styrene) (SIS) and sealed along the sensors edges with polydimethylsiloxane (PDMS). As illustrated at the bottom of Fig. 1d, the overlapping plates slide in opposing directions when the sensor is strained. The sliding of plates shifts the alignment of overlapping fingers, decreases the overlapping area, and causes a decrease in capacitance. The miniaturized strain sensor employing stretchable interconnects is imaged in Fig. 1d on a set of tweezers. The sensor is integrated onto a wireless stent platform to enable wireless

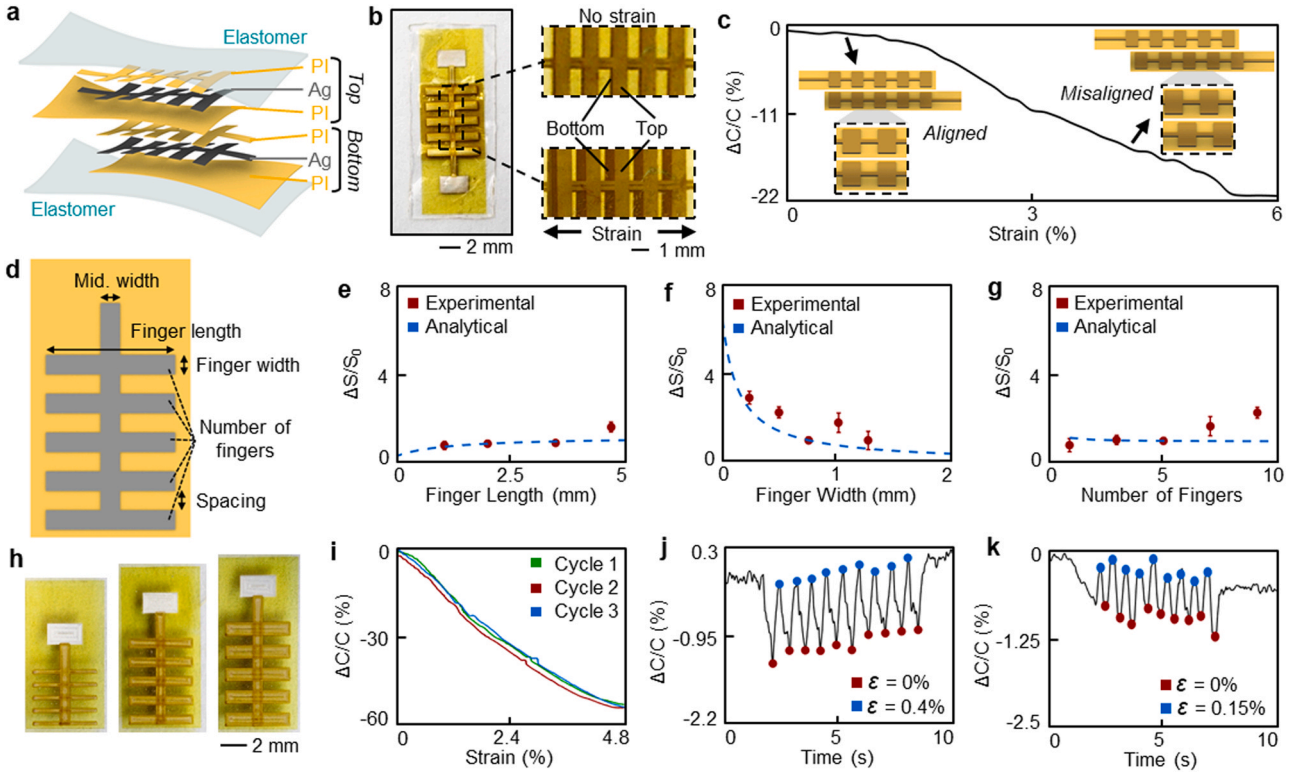

Fig. 2. Characterization and optimization of membrane strain sensors that use a sliding mechanism. (a) Exploded view of a strain sensor consisting of PI and AgNP layers encapsulated in elastomeric membranes. (b) Photo of an assembled strain sensor (left) with images showing the shifting of plates with and without strain (right). (c) Change in capacitance of a sensor from 0% to 6% strain. Inset illustrations show the shifting of plates as strain is increased. (d) Critical design features of the strain sensor. (e-g) Optimization results of strain sensor for (e) finger length, (f) finger width, and (g) number of fingers. Strain sensitivity is improved by increasing finger length and decreasing finger width. Increasing the number of fingers shows a minimal increase in sensitivity. Experimental results compare well with trends predicted by an analytical model of sensitivity. (h) Photos of three different strain sensors using different finger widths. (i) Optimized strain sensors show high sensitivity with a 60% change in capacitance at a strain of 4.8%. (j-k) Capacitance change is observed for strains as low as (j) 0.4% and (k) 0.15%.

communication from an artery. The wireless stent uses a multi-material structure of stainless steel (SS), PI, gold (Au), and parylene (Fig. 1e). The stent is laser machined to have SS loops and microscale PI connectors prior to electroplating the structure with Au and insulating in parylene (details in Methods and Fig. A.2). As illustrated in Fig. 1e, this enables a current flow resembling a solenoid inductor and allows the stent to function as an inductive antenna. A key advance of the stent design is using the 'S' shaped PI connectors that offer mechanics similar to conventional stents while enabling wireless functionality. Fig. 1e also shows an image of the stent in an unexpanded form with an enlarged view of the PI connector. The integrated set of a stent and a sensor is expandable with a balloon catheter for minimally invasive implantation. Fig. 1f shows the expanded device with an enlarged view of the strain sensor. Owing to the low-profile form and flexible mechanics, the sensor is implantable into narrow arteries, as shown by the sensor implanted in the coronary artery of an ovine heart in Fig. 1g.

Characterization and optimization of membrane strain sensors that use a sliding mechanism

Strain sensor design was investigated to enable high sensitivity and low strain detection in order to detect minute changes in arterial stiffness. To enable passive sensing, a capacitive strain sensor design was utilized. Numerous studies of soft capacitive strain sensors employ a sensing mechanism based on the Poisson effect, where the dielectric layer changes dimensions under strain [46–56]. However, this mechanism theoretically limits the sensitivity to around a gauge factor of 1 [57]. In order to enhance sensitivity and detection of low strains, an alternative is to employ a sliding mechanism where overlapping plates slide relative to each other [58]. Here, plates consisting of a set of fingers are fabricated with AgNPs and aligned to form a soft strain sensor with high sensitivity. Fig. 2a illustrates an exploded view of the strain sensor consisting of top and bottom plates encapsulated in elastomers. Both plates are aerosol jet printed to have a bottom PI layer, middle AgNP layer, and a top PI layer (details in Fig. A.1 and Video A.1). The two identical plates are aligned on top of each other, with the extended bottom PI layer orientated in opposite directions along the length of the sensor. This orientation allows the two PI base layers to be pulled in opposite directions as the elastomer is stretched. Fig. 2b displays an assembled strain sensor and depicts the sliding mechanism where the overlapping fingers shift during strain (Video A.2). As shown in Fig. 2c, the shifting of plates during strain causes a decrease in capacitance as the overlapping area decreases (Fig. A.3). To enhance sensitivity, optimization of strain sensor design was investigated in terms of finger dimensions (Fig. 2d). Key parameters were determined to be finger length (L), finger width (x), and number of fingers (N). The spacing of fingers (y) does not impact sensitivity but rather dictates the maximum strain that can be detected, which occurs when the fingers begin to re-overlap. Middle electrode width (d), which is the width of the line connecting all fingers, can be eliminated by offsetting the connection to prevent overlap between two plates. Using these parameters, an analytical model to predict capacitance change ($\Delta C/C$) for a given strain was developed (details in Note A.1):

Supplementary material related to this article can be found online at doi:10.1016/j.nantod.2022.101557.

Using this analytical model, the effects of all finger dimensions were evaluated. Total sensor length (L_{total}) and strain (ε) are included

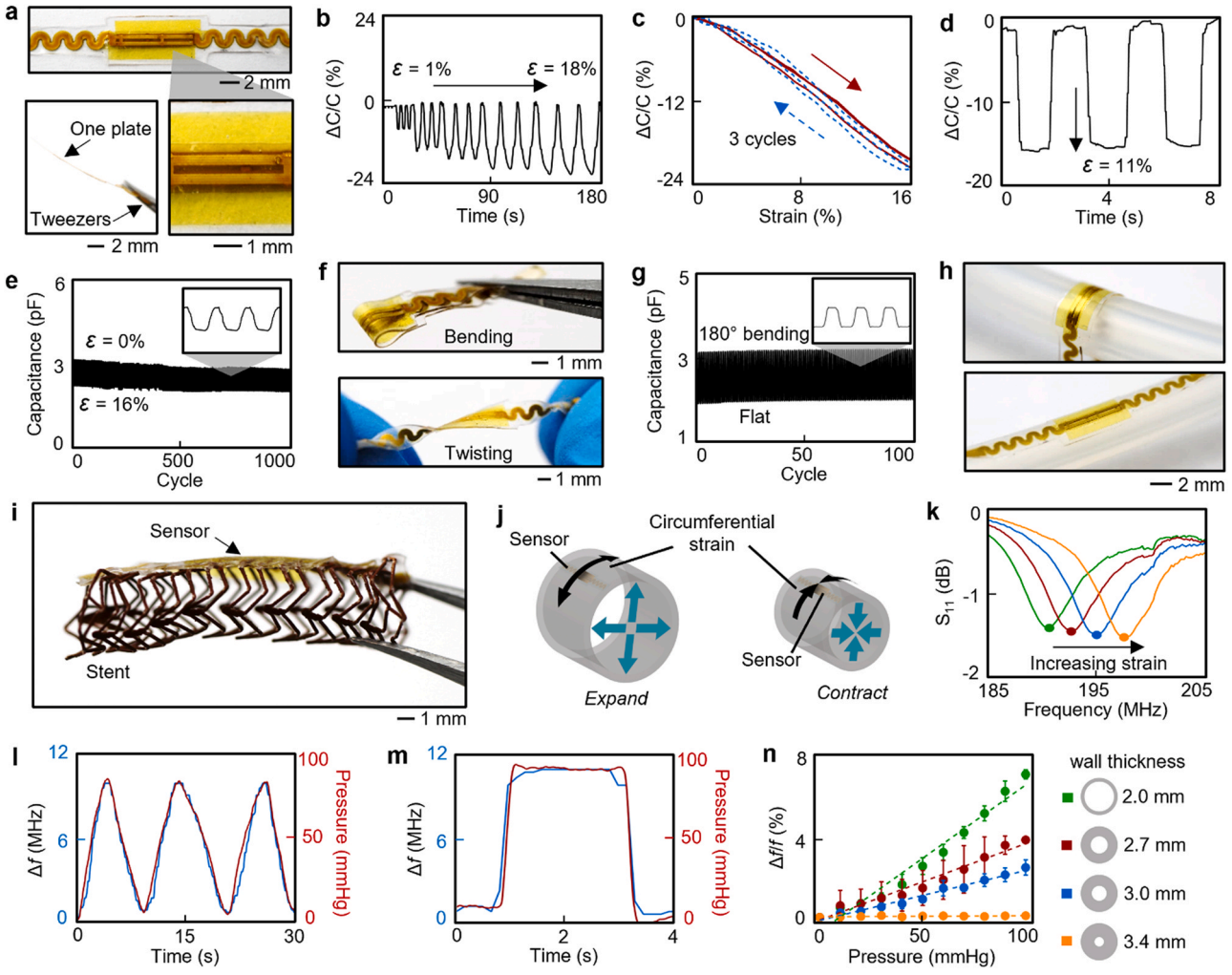

Fig. 3. Mechanics and functions of strain sensors for arterial stiffness monitoring. (a) Photo of a strain sensor for restenosis monitoring with an enlarged view displaying a thin, printed plate and the overlapping two fingers of the miniaturized sensor. (b) Capacitance change of a restenosis sensor during cyclic strain changes at increasing levels. (c) Capacitance change of the sensor in (b) from a strain of 0–16% indicates minimal hysteresis. (d) The strain sensor shows an immediate response to significant strain changes. (e) Capacitance changes of the sensor during cyclic strain from 0–16% strain for 1000 cycles. (f) Photos of the thin-film strain sensor demonstrating high flexibility during bending and twisting. (g) Capacitance changes showing enhanced stability during cyclic 180° bending of strain sensor. (h-i) Photo of a strain sensor showing conformal lamination (h) on curved surfaces and (i) onto a wireless stent. Integrating the stent and sensor forms the wireless device. (j) Illustration depicting strain sensor location for monitoring circumferential strain in the tubing. (k) Wireless S_{11} signals from the integrated stent and strain sensor showing the shift in resonant frequency as strain is increased. (l) Resonant frequency of wireless device detecting circumferential strain from a silicone tube as pressure is changed. An increase in pressure expands the tubing and causes an increase in strain. (m) Wireless sensing displays a fast response time. (n) Summary of resonant frequency change with increased pressures for 4 different tubing wall thicknesses. A decrease in the resonance change with pressure is observed as tubing wall thickness increases since it stiffens the tubing.

in the model. Finger length, finger width, and number of fingers were identified as critical to sensitivity and size of the sensor. To validate the analytical model, strain sensors were printed and assembled with variations in finger dimensions (Fig. A.4). A baseline sensor was fabricated using five fingers with a width of 0.75 mm and length of 5 mm. All sensors maintained a total length of 25.6 mm, measured from the edges of the PI plates. Strain sensors were tested from 0% to 4.8% linear strain, and an overall sensitivity was determined (Fig. A.5). The strain range was selected to more than encompass expected strains of a normal, healthy coronary artery which have been previously reported with varying values, including arterial strains of 2.9% and 3.8% calculated from lumen area and diameter changes [59–61]. The healthy coronary artery case results in the largest strain to be measured as stenting and restenosis increases arterial stiffness. The baseline sensor displayed a gauge factor of 3.7. Fig. 2e displays the impact of finger length, where both analytical and experimental trends show a slight increase in sensitivity. The sensitivity values shown are normalized to the baseline sensor. As shown in Fig. 2f, finger width displays the largest impact on sensitivity, where a smaller finger width enhances sensitivity. A finger width of 0.25 mm offers a 3-times improvement in sensitivity compared to a finger width of 0.75 mm. Fig. 2g indicates a larger number of fingers showed a moderate increase in sensitivity. Based on these results, fewer and more narrow fingers may be used to achieve a miniaturized strain sensor while maintaining a high sensitivity. This size change is highlighted in Fig. 2h showing a representative set of printed plates using different finger widths. Although the narrowest fingers offer the smallest size, it offers greater sensitivity than the larger ones. The narrowest fingers achieved a sensitivity as high as 10.5 and the sensor capacitance for 3 different stretching cycles is shown in Fig. 2i. The sensor achieved a 60% change in capacitance with less than 5% strain. This sensitivity is approximately 10-times greater than the sensitivity typically achieved by soft capacitive strain sensors relying on the Poisson effect design and 3-times greater than a previously reported sliding strain sensor (Table A.1) [46–56,58]. In addition to high sensitivity,

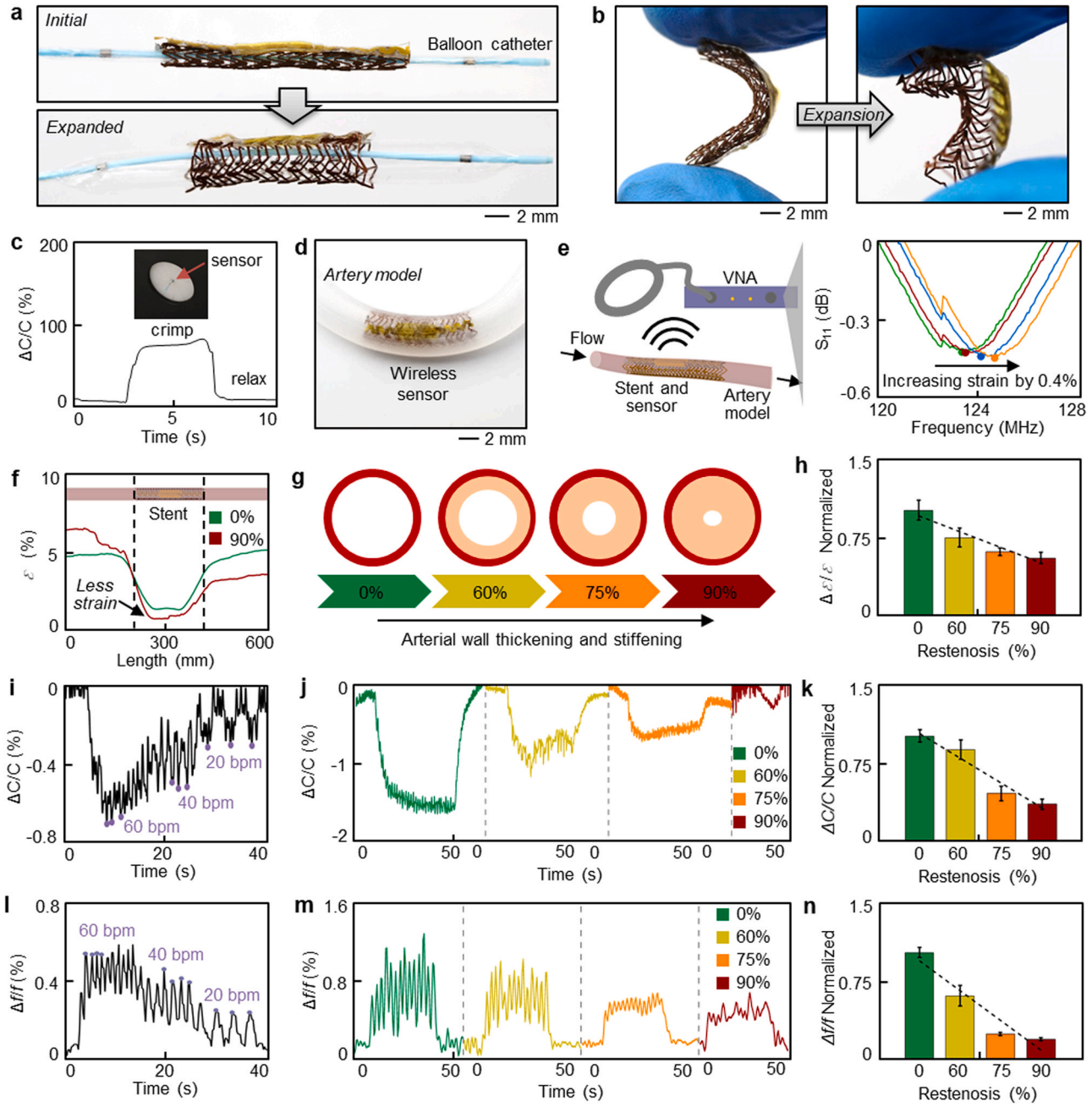

Fig. 4. Restenosis sensing in artery model with sensors integrated in a stent. (a) Photos of integrated stent and strain sensor before and after expansion with a balloon catheter. (b) Photos of implantable device demonstrating high flexibility before and after expansion. (c) Capacitance of sensor during crimping of stent and sensor onto balloon catheter. The sensor endures crimping and returns to a baseline capacitance after release. (d) Photo of the device deployed in artery model. (e) Schematic of wireless sensing system using VNA to record S_{11} of stent and sensor circuit. The resonant frequency changes with arterial strain. (f) Arterial strain measured optically showing a decrease in strain in the stented region. Strain in the stented region decreases further as restenosis progresses. (g) Illustration of wall thickening and stiffening as restenosis progresses from 0% to 90%. (h) Average strain optically measured across the stented region showing a decreasing strain at higher restenosis levels. (i) Sensor capacitance during pulsatile flow within artery model. (j) Sensor capacitance during pulsatile flow at four restenosis levels. A smaller change in capacitance occurs as restenosis increases due to stiffening of the artery. (k) Summary of capacitance change during the progression of restenosis. (l) Resonant frequency of wireless sensor during pulsatile flow in artery model. (m) Resonant frequency changes of the sensor at each restenosis level. An increase in restenosis causes smaller changes in resonant frequency. (n) Summary of resonant frequency change at each restenosis level.

the strain sensor enables the detection of small strain changes. Fig. 2j shows detection of cyclic, 0.4% strain changes, while Fig. 2k shows 0.15% strain changes, which was the lowest strain achievable by the testing equipment. The strain sensor exhibits a 1.11% and 0.63% change in capacitance for the 0.4% and 0.15% strain changes, respectively. The baseline of the raw capacitance signal of the sensor shows shifts of 0.29% and 0.42% in Fig. 2j and k, respectively. The shift in baseline capacitance may arise from slipping of elastomer within the testing clamps (Fig. A.3g), shifting or misalignment of fingers during stretching, and operating the motorized stretch stand near its minimum resolution. Signal processing can be applied to minimize the baseline trend, which resulted in lowered baseline changes of 0.04% and 0.10% (Fig. A.6). The fluctuations in amplitude change for the 0.15% strain cycles indicate the sensor operating near its sensing limit and the motorized stretching stand operating near its minimum resolution.

Mechanics and functions of strain sensors for arterial stiffness monitoring

Criteria based on the sensor optimization results were applied to develop a miniaturized strain sensor for integration with a stent and sensing of arterial stiffness. Fig. 3a displays the miniaturized vascular sensor design for restenosis sensing using stretchable, serpentine interconnections. With respect to the photo in Fig. 3a, the sensor fingers slide vertically to detect strain changes. The sensor uses 2 fingers with a width of 0.3 mm and length of 7.5 mm to achieve high sensitivity at a small, narrow size. Fig. 3a also displays a side view of a thin printed plate to highlight the low-profile compatibility with implantation. The soft miniaturized strain sensor shows a sensitivity over 1.5 despite a sensing area with a length of 3 mm (Fig. A.7). The sensor displays a stable performance, as shown in Fig. 3b. No hysteresis is observed as strain continuously changes on the sensor (Fig. 3c). Since the sensor is required to respond to quick, cyclic changes in strain, it is critical the sensor displays a fast response time. As shown in Fig. 3d, the sensor displays immediate changes in capacitance despite sudden stretching to 11% strain. Coupled with the high sensitivity, the sensor shows stable operation over 1000 cycles of significant strain changes from 0% to 16% (Fig. 3e). The sensor was evaluated at strains that more than sufficiently cover the maximum expected artery wall strains of 2–5% [59,60,62]. Along with sensitivity, the sensor is required to be highly flexible and durable for implantation into an artery and to interface with compliant artery walls. As imaged in Fig. 3f, the sensor displays high flexibility as it folds onto itself and twists without failure. The sensor shows no change in baseline capacitance after 100 cycles of 180° bending to a radius of 0.5 mm (Fig. 3g). Additionally, the resistance of the AgNP remains unchanged during cyclic bending (Fig. A.7). Owing to the flexibility of the sensor, the sensor seamlessly conforms to curved surfaces as shown by the photos of a sensor on silicone tubing in Fig. 3h. This conformal contact is critical to the integration with a stent to form a low-profile device and to interface unobtrusively with soft artery walls. As a result, the sensor is well suited to be laminated onto the wireless stent, as shown by the integrated device in Fig. 3i. Based on the orientation of the sensor, circumferential strain of the stent is measured by the sensor, as illustrated in Fig. 3j. The sensor is electrically connected at the two ends of the stent with silver paint and insulated with PDMS. Soft tubing was used to validate sensing of circumferential, or tubing wall, strain as the tubing expands and contracts with internal pressure changes. Pressure within the tubing is monitored and controlled, where an increase in pressure causes expansion of the tubing, simulating the distensibility of an expanding artery. Resonant frequency of the wireless stent and sensor system was measured with a vector network analyzer (VNA) monitoring the S_{11} parameter. Resonant frequency is identified as the frequency where the S_{11} parameter is at a minimum. The resonance frequency shifts with a change in sensor capacitance. In this work, the S_{11} parameter is monitored directly from the VNA as has been shown in prior demonstrations of passive, wireless sensors [25,63,64]. The real part of impedance is another method that may be used to measure resonant frequency (Fig. A.8b). Due to the 'S′ shaped polyimide connector, the inductive stent shows a parasitic capacitance of 0.8 pF. Self-resonance of the stents were measured to calculate parasitic capacitances (details in Note A.2; Fig. A.8c). Capacitive sensors averaged baseline capacitances of 5 pF, and are able to be increased up to 10 pF with the use of a laminating press to compress and align sensor fingers together during sensor sealing with elastomer. Variations in sensor assembly occur due to manual alignment of sensor fingers and sealing, which can cause sensor baseline capacitances to range from 2 pF to 10 pF, but the application of a laminating press reduced variability between sensors. In addition, quality factor of the combined stent and sensor was measured to be 16 (details in Note A.2; Fig. A.8e). A coupling constant of 1.1×10^{-3} between the wireless device and antenna was determined (details in Note A.2). Stent inductances and resistances averaged 450 nH and 4.5 Ω. Wireless devices consisting of stent and sensor averaged resonant frequencies of 110 MHz, but ranged from a minimum of 80 MHz to a maximum of 200 MHz throughout this study due to the variations in stent inductance and sensor capacitance. As shown in Fig. 3k, an increase in strain caused resonant frequency to increase from 190 MHz to 198 MHz due to the decreasing capacitance of the strain sensor. Continuously monitoring resonant frequency enables real-time detection of strain changes within the tubing, as highlighted in Fig. 3l where an approximate 10 MHz change is realized for a 90 mmHg change in pressure (Fig. A.9). Owing to the immediate response time of the strain sensor, a fast response time is observed wirelessly as shown in Fig. 3m. The wireless sensor embedded in soft tubing was further demonstrated by detecting wall strains for different tubing wall thicknesses. A thicker wall tubing will show less strain at a given pressure compared to a thinner wall tubing (details in Fig. A.10). As shown in Fig. 3n, the wireless sensor shows a larger change in resonance for thinner tubing walls. The response correlates well with the expected decrease in distensibility and strain as tubing walls thicken. The decrease in distensibility with thickening tubing walls has been previously observed in the development of arterial models [65–67]. The restenosis model applied here has been computationally shown previously and is experimentally measured optically during pulsatile flow in the next section [68]. Additionally, low strain changes stemming from low pressure changes (< 30 mmHg) were detected by the sensor, which is critical for operation in coronary arteries (Fig. A.11). This soft tubing model mimics the progression of restenosis where arterial walls thicken, which validates the potential of the wireless sensor for arterial stiffness sensing.

Restenosis sensing in artery model with sensors integrated in a stent

Based on the capability to detect tubing distensibility, the wireless sensor is well suited for monitoring arterial stiffness. To enable implantation into arteries, the integrated stent and sensor were developed to be compatible with conventional catheterization procedures. As shown in Fig. 4a, the integrated device is able to be mounted onto a balloon catheter and expanded. The stent uses a length of 25 mm and starts at a 2 mm diameter and expands up to a 4.8 mm diameter. In both unexpanded and expanded forms, the device demonstrates a high flexibility which is critical for guiding through narrow, curved arteries to the target location (Fig. 4b). In addition to flexibility, the device demonstrates mechanical durability, as indicated by the crimping of the stent and sensor onto a balloon catheter in Fig. 4c. Crimping is a common process for stents and ensures proper mounting onto a balloon catheter. The application of high force increases sensor capacitance but the sensor returns to a baseline capacitance shortly after release. During expansion, the parylene coating is deformed as the stent pattern expands. The parylene layer was examined at the arcs of the stent pattern, which are the locations of highest strain, but signs of cracking were not observed (Fig. A.12). Additionally, resistance of the stent changed by less than 0.9% when submerged in saline, indicating insulation from the surrounding conductive fluid. To demonstrate arterial stiffness sensing to quantify restenosis, a soft artery model was developed and validated experimentally and computationally [68]. The artery model used a wall thickness of 2 mm and an inner diameter of 4 mm to achieve the biomimetic performance of coronary arteries. The wireless stent and sensor was expanded and implanted into the artery model, as shown in Fig. 4d. Pulsatile flow was applied within the artery model while resonant frequency of the implanted device was monitored with a VNA and loop antenna (Fig. 4e, Fig. A.13). As flow changes, expansion and contraction of the artery occur and are

detected by changes in resonant frequency, as shown by the frequency sweeps in Fig. 4e. The wireless stent and sensor were characterized to measure readout distance in both air and saline (Fig. A.14a-d). Resonant frequency was detected in air up to 2.5 cm and 1.0 cm in the radial and axial directions, respectively. While this paper focused on the implantable device, ongoing work to develop an improved external antenna, electronics, and readout system will increase the communication distance for future in vivo demonstrations. The use of an untuned loop antenna and VNA limits measuring the wireless sensor's readout distance. As distance increases, the change in magnitude of the S_{11} parameter decreased. When operating in a 0.08 M saline solution, matching the blood conductivity, the distance decreased to 1.5 cm and 0.5 cm in the radial and axial directions, respectively (Fig. A.14e) [69–71]. Saline causes a decrease in resonant frequency and dampens the signal due to the conductivity of the surrounding medium and capacitive damping effects on the stent [72]. Future work on additional insulations will be performed to improve performance for in vivo conditions where the device will operate in blood and tissues and the wireless signals will be dampened. In addition to distance, the impact of alignment between external antenna and stent was evaluated (Fig. A.14f-i). Rotation of the stent with respect to the antenna causes a decrease in the signal amplitude at resonance before becoming unreadable at a 90°, or perpendicular, rotation. Additionally, the concentric alignment was evaluated and did not show changes, which may be due to the initially low coupling efficiency between antenna and stent. For in vivo application, the impact of alignment will need to be considered depending on artery location and orientation towards the skin. The artery model was applied to demonstrate the detection of restenosis with both the wired capacitive strain sensor and the integrated wireless device. The wired capacitive sensor results are included to directly observe the strain sensor capacitance. To quantify the change in stiffness stemming from restenosis, an optical measurement system was developed to measure arterial strain changes at 0%, 60%, 75%, and 90% restenosis levels. These restenosis levels were selected as 0% for a healthy artery while restenosis becomes significant as it increases from 60% to 75% and higher. Optical strain measurements were performed to quantify the arterial stiffness along the length of the artery during a flow rate of 60 mL min^{-1} using 60 b.p.m (Video A.3). The measured arterial strain correlated with the applied pulsatile flow in the artery model (Fig. A.15). Optical measurements indicated the stented region of the artery showed less strain than the artery before and after the stent, which is due to the stent locally stiffening the artery. This stiffening can be observed when measuring the strain along the entire length of the artery at different time points during a pulsatile wave (Fig. A.15). Importantly, the pulsatile strain along the stented region decreases further when restenosis progresses, as shown in Fig. 4f for a healthy artery and an artery with 90% restenosis. Fig. 4g illustrates the cross-sectional view of restenosis at the 4 restenosis cases, where a thickening of the artery decreases strain. A summary of the strain changes, normalized to a healthy artery, is shown Fig. 4h for each restenosis case. The summarized values are determined by measuring the amplitude of pulsatile strain change during flow (Fig. A.15f-i). Deviations in optically measured strain result from differences in stent stiffness due to fabrication variations.

Supplementary material related to this article can be found online at doi:10.1016/j.nantod.2022.101557.

The measured change in arterial stiffness was used to validate the arterial stiffness sensor. Fig. 4i shows the capacitance of a wired sensor during pulsatile flow at 3 flow rates. While the implantable device is a wireless one, here the wired sensor was separately characterized to directly validate the capacitive strain sensor performance for restenosis monitoring and to measure sensor capacitance independently from the wireless stent. The sensor captures the pulsatile waveform of the artery expanding and contracting during the changes in flow rate and pressure (Fig. A.16). The sensor indicates a 0.8% change in capacitance for a flow rate of 60 mL min^{-1}. As restenosis is introduced into the artery model, a decrease in capacitance change is observed from 0% to 90% restenosis for the same flow rate of 60 mL min^{-1} (Fig. 4j). Fig. 4k summarizes the capacitance changes normalized to the healthy artery. The capacitance changes were measured as the average amplitude of capacitance change (Fig. A.16). Owing to the softness of the sensor, the alignment of the overlapping fingers in the strain sensor was susceptible to shifting during implantation into the artery model and could lead to an inverted signal, where capacitance increases with small levels of strain as the shifted fingers realign (Fig. A.17). This misalignment was also noted when linearly stretching the larger strain sensors at small strains. Similar to the optical measurements, the wired sensor shows a larger change from 60% to 75% restenosis and compares well with the trends in Fig. 4h. A 60% restenosis shows a 12% decrease in capacitance changes from a normal artery. A larger change is observed for a 75% and 90% restenosis with a 40% and 62% decrease in capacitance changes, respectively. Wireless signals were similarly recorded from an implanted wireless device (Fig. A.18). Fig. 4l shows resonant frequency changes over time at 3 different flow rates and is timed to correlate with wired capacitance measurements previously shown in Fig. 4i. Fig. 4m shows resonant frequency changes at a 60 mL min^{-1} flow rate for each restenosis stage. As restenosis increases, the change in capacitance decreases and causes a decrease in overall resonant frequency change. Importantly, the inductance of the stent showed minor changes and confirms resonance is being shifted by the capacitive sensor (Fig. A.18g). Additionally, the electrical connection between the stent and sensor during flow was measured (Fig. A.18h). Resistance was measured from the strain sensor fingers, which allows for measuring of resistance across the serpentine sensor interconnections, the stent, and the two connection points between sensor and stent. Baseline resistance was 4.7 Ω and the maximum fluctuation observed was 0.27 Ω corresponding to a 5.7% fluctuation. Fluctuations correlated with pulsatile flow indicating an impact of conductive fluid flow along the device. The intrusive attachment of wires through encapsulation of the device within the artery model may increase the shifts in resistance compared to an enclosed, wireless device. Resonant frequency changes were compared based on the average amplitude change and normalized to the healthy artery case (Fig. 4n). Similar to wired capacitance measurements, when sensors were misaligned during implantation, the resonant frequency changes were inverted (Fig. A.17). Fig. 4n shows a similar trend to the wired measurements with a large decrease detected from 60% to 75% restenosis. A 35% decrease in resonance changes was observed when introducing a 60% restenosis to a healthy artery. For 75% and 90% restenosis cases, a 63% and 68% decrease in resonance changes were detected. Overall, the artery model validates the use of arterial stiffness sensing and the wireless electronics to quantify clinically relevant stages of restenosis. Compared to prior works, this is the first demonstration of a stent-based arterial stiffness sensor and wireless arterial stiffness sensing (Table 1)[28,32,34–36]. Prior works in Table 1 were selected based on if they measured arterial stiffness, monitored changes in movement of arterial walls, or discussed restenosis as a target application. By integrating a wireless stent platform with the enhanced soft, capacitive strain sensor, wireless arterial stiffness sensing is achieved while enabling minimally invasive implantation via a catheter. The reported sensor offers advancements in arterial stiffness sensing in order to quantify restenosis and offers broader potential for cardiovascular health monitoring.

In addition to restenosis monitoring, the long-term stability of the sensor and stent were briefly characterized. Long-term stability tests were performed in saline at a temperature of 62 °C to accelerate

Table 1
Comparison of implantable sensors for restenosis, occlusion, and arterial stiffness monitoring.

Reference	Target parameter	Wireless / sensor	Implantation method	Sensitivity	Measured progression of occlusion	Real-time detection	Monitoring target
This work	*Arterial stiffness*	*Yes / flow and pressure*	*Catheterization*	*6.8% / mm* *0.071% / mmHg*	*Yes*	*Wireless* *- Ex Vivo*	*Restenosis*
[36]	Arterial stiffness	No	Open surgery	133% / mm[a]	No[b]	Wired / open body – in vivo	Stiffness
[34]	Arterial stiffness	No	Open surgery	0.061% / mmHg[c]	No	Wired / open body – in vivo	Pressure
[32]	Blood pressure gradient	Yes / pressure	Catheterization	No data	No	No	–
[28]	Blood pressure	Yes / pressure	Catheterization	No data	No	Wireless / open body – in vivo[d]	Clot[e]
[35]	Pressure exerted by artery	Yes / pressure	Open surgery	No data	Yes	Wireless / open body – in vivo	Occlusion

[a] Sensitivity is determined from a scaled sensor signal related to photodetector output voltage.
[b] Measured stiffness changes from the administration of dopamine.
[c] Strain sensor is characterized by comparing capacitance changes with arterial pressure.
[d] Device implanted in a graft and then implanted using a bypass procedure.
[e] Measured a signal change from a healthy artery to a fully occluded artery.

testing. At this temperature, an aging factor of 5.6 is applied, where a 9 day test is equivalent to 50 days implanted [73]. The capacitive strain sensor was characterized using two different elastomers: PDMS and SIS (Fig. A.19). SIS was included as it has been previously shown to be a superior fluid barrier compared to PDMS [74]. A key concern of the capacitive sensor when operating in a conductive fluid is swelling of the encapsulation and permeation of fluid that disrupts sensing and may cause shorting, although the printed PI helps insulate individual conductive traces. Conductance was monitored over the test period, where PDMS encapsulated sensors showed an increase in conductance from 0.22 µS to 272 µS while SIS demonstrated a more stable conductance in changing from 0.36 µS to 3.59 µS (Fig. A.19). Similarly, PDMS sensors increased in baseline capacitance from 4.1 pF to 151.2 pF while SIS sensors showed a lower change from 6.7 pF to 14.6 pF (Fig. A.19). As a result, the SIS encapsulated sensors maintained sensing of strain but with varying decreases in sensitivity over time until no detectable change in capacitance was observed during stretching. SIS encapsulated sensors were sealed along the edges with PDMS and this PDMS sealant was observed to detach from the SIS films over time when manually handled, which would introduce additional fluid permeation. The use of SIS to seal the sensor may minimize this leakage. In addition to capacitive sensors, stents and wireless devices were evaluated (Fig. A.20). Resistance of the stent during pulsatile flow showed fluctuations over time, presumably disrupting the electrical connection of the monitoring wires and sensor wires to the stent where the electrical connections had been coated with only PDMS (Fig. A.20). Wireless signals fluctuated between samples when in saline over time, but changes in strain from the artery model could still be observed until day 9 with degrading signal quality (Fig. A.20). Future work will be performed to add improved encapsulation materials upon the device design and sensing strategy presented here. While the demonstrations of long-term performance is limited, future application of multi-layered encapsulations, previously developed in other works may be used to improve long-term stability for longer test periods [75–79]. Such encapsulations include integrating additional material layers with the existing parylene on the current stent. Integrating improved coatings with the currently presented stent and sensor designs will be performed to improve long-term capabilities and enable long-term in vivo evaluations.

Ex-vivo ovine study of restenosis sensing

An ex-vivo study with ovine hearts demonstrated sensing of stiffness changes in soft arteries. The study was performed to demonstrate the wireless arterial sensor can be implanted and operated in soft tissue in addition to the silicone artery model. Fig. 5a shows an ovine heart and indicates one of the coronary arteries used for implantation (Fig. A.21). A wired sensor was implanted into a coronary artery to validate the ability of the capacitive sensor to detect arterial strain, as imaged in Fig. 5b with an enlarged view of the soft sensor. As shown in Fig. 5c, changes in capacitance were observed between no flow and flow conditions (Fig. A.22). Importantly, the capacitance displays a characteristic waveform showing systole and diastole regions of the pulsatile wave (Fig. 5d). Conditions of no restenosis and restenosis were introduced to the coronary artery of the ovine heart, as imaged in Fig. 5e. Silicone was added to the artery to stiffen the region near the implanted sensor. As shown by capacitance signals in Fig. 5f, restenosis causes a decrease in the change of capacitance for identical flow conditions. In both cases, the sensor showed the pulsatile waveform, detection of flow changes, and identified pulse rates similar to the flow setting of 20 and 30 b.p.m. Fig. 5g summarizes the detected stiffness changes between a healthy artery and an artery with restenosis at 2 different flow rates. Capacitance changes were measured as the average amplitude of during flow and normalized to the normal artery. At the

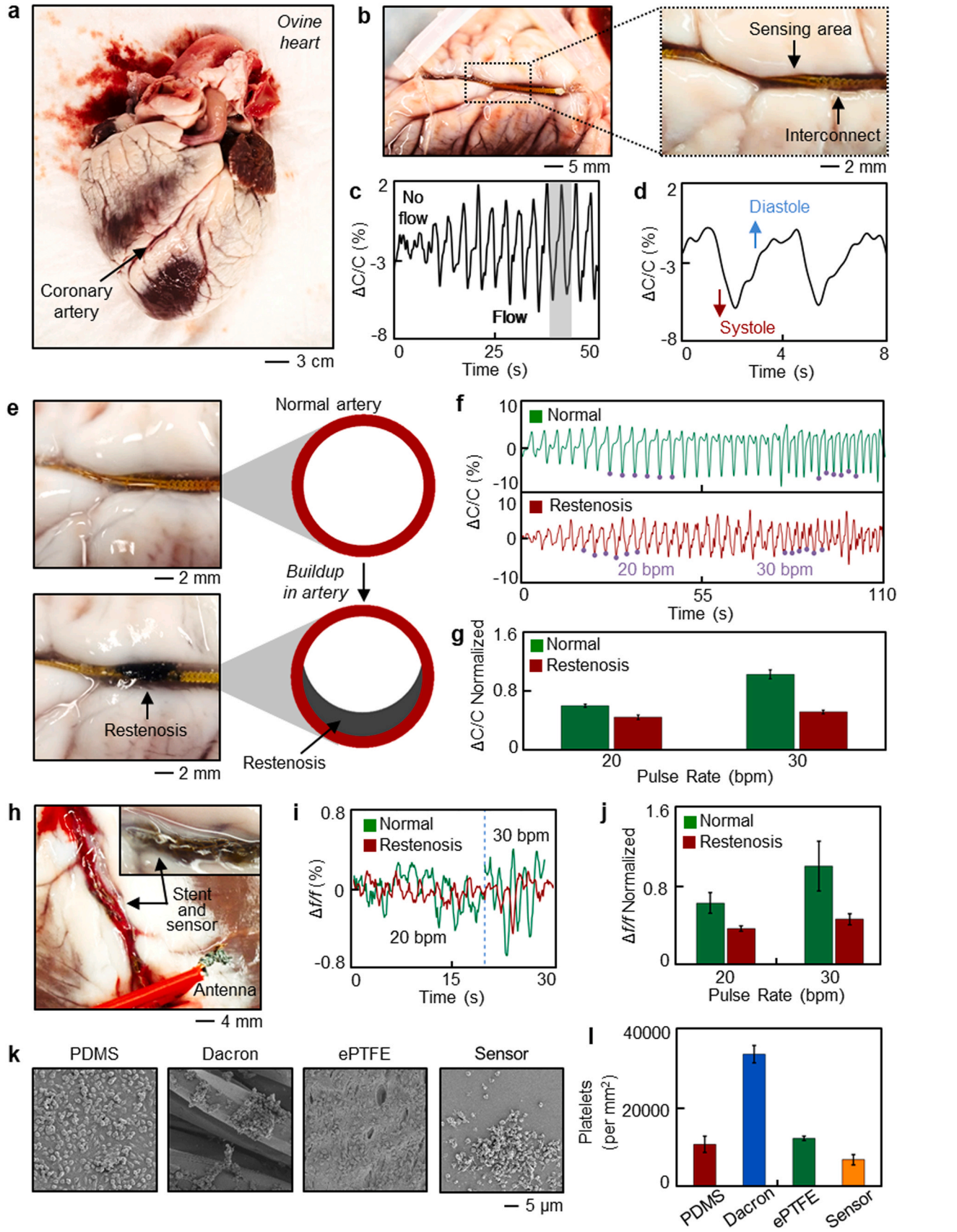

(caption on next page)

Fig. 5. Ex-vivo ovine study of restenosis sensing. (a) Photo of ovine heart used to demonstrate restenosis sensing. (b) Restenosis sensor implanted in a coronary artery of the ovine heart with an enlarged view showing the sensing area and interconnectors. (c) Capacitance change of the implanted sensor during pulsatile flow with (d) an enlarged view of a waveform. (e) Photos of implanted strain in a normal artery (top) and artery with restenosis (bottom). Illustrations show the cross-section of the artery. (f) Capacitance of sensor at two flow rates from an artery with and without restenosis. A lower change in capacitance occurs in the artery with restenosis due to stiffening of the artery. (g) Summary of capacitance changes before and after restenosis occurs at 2 different flow rates. (h) Wireless stent and sensor implanted in a coronary artery with blood flow. (i) Wireless signal of stent and sensor showing resonant frequency change between flow conditions and with and without restenosis. (j) Summary of resonant frequency changes at different flow rates in the artery with and without restenosis. A smaller shift in resonant frequency occurs as the artery is stiffened by restenosis. (k) SEM images showing hemocompatibility of the strain sensor compared to controls with deposited platelets. (l) LDH assay of samples in (k) after contact with citrated fresh ovine whole blood.

higher flow rate a 46% decrease in capacitance change occurs due to restenosis and at the lower flow rate a 39% decrease in capacitance change occurs due to restenosis. In addition, wireless sensing was demonstrated in the coronary arteries of the ovine heart (Fig. A.23). The integrated stent and sensor were implanted in the artery, as shown in Fig. 5h. The external antenna was placed within 1 cm of the device to monitor the device and wirelessly detected resonance changes, as shown in Fig. 5i. A device in an artery with restenosis displayed lower changes in resonant frequency compared to the normal artery. The resonance changes are summarized in Fig. 5j after normalizing resonance amplitude changes to that of the normal artery. Wireless results compare well with the trends observed from the wired capacitive sensors. The ex-vivo study demonstrates strain sensing within soft arterial tissue. Future in vivo demonstrations will require guiding the stent and sensor through arteries on a catheter and will require an improved external electronic system to wirelessly couple with an implanted device. Additionally, the soft sensor was evaluated for biocompatibility and hemocompatibility using rat vascular smooth muscle cells and ovine blood (Fig. A.24). Fig. 5k displays scanning electron microscopy (SEM) images of the strain sensor surface along with three established biocompatible materials of polydimethylsiloxane (PDMS), polyethylene terephthalate fabric (Dacron), and polytetrafluoroethylene (ePTFE). SEM images indicate the degree of aggregation and adhesion areas of the platelets to the surfaces. PDMS and ePTFE shows a consistent number of platelets across its surface while Dacron shows more aggregation. The encapsulated sensors shows a lower and less widespread platelet deposition, indicating greater hemocompatibility. Platelet deposition was quantified by lactate dehydrogenase (LDH) assay after contact with ovine blood and is summarized in Fig. 5l. Results indicate hemocompatibility of the sensor and the potential of the wireless sensor for arterial stiffness and restenosis monitoring.

Conclusion

We have demonstrated an implantable arterial stiffness sensor system comprised of soft strain sensors and an electronic stent for the detection of restenosis. A capacitive strain sensor is designed and optimized to use a sliding sensing mechanism to improve both sensitivity and low strain detection at a miniaturized size. This sensor design and printed nanomaterials offer significant improvements for capacitive strain sensing. The aerosol jet printed strain sensor seamlessly integrates with an inductive stent to enable wireless sensing of arterial stiffness. The wireless device is demonstrated for unobtrusive monitoring of restenosis in a biomimetic artery model and in an ex-vivo study with ovine hearts. Overall, the reported advancements in capacitive strain sensing and wireless integration extend battery-free vascular electronics capabilities and enable monitoring of arterial stiffness and restenosis progression. The wireless arterial stiffness sensing electronics presented here offers broader potential for monitoring arterial stiffness for predicting and monitoring cardiovascular health. Future work will include improving encapsulation materials and strategies to improve long-term stability of the device, modifying sensor encapsulations towards thinner sensors, investigating pressure-related effects of the sensor within the artery wall, and an in-vivo study of restenosis monitoring.

Experimental section

Microfabrication of strain sensor

An aerosol jet system (Optomec, Aerosol Jet 200) was used to print strain sensors. A glass slide was coated with a layer of polymethyl-methacrylate (PMMA; MicroChem) by spin-coating at 3000 r.p.m. for 30 s and cured for 3 min at 180 °C. A bottom PI layer was printed using ink consisting of PI (HD MicroSystems, PI-2545) and 1-methyl-2-pyrrolidinone (NMP, Sigma Aldrich) mixed at a 3.5:1 ratio. The bottom PI layer was cured for 1 h at 240 °C. The cured PI was plasma treated prior to printing AgNP ink (UTDOTS, AgNP40X). The printed AgNP layer was sintered for 1 h at 240 °C. A top PI layer was printed and cured similar to the bottom PI layer. The bottom and top plates are printed separately on the same glass slide using identical printing parameters. After printing, the PMMA layer is removed by covering the glass slide and placing it in acetone for over 1 h. The printed sensor plates are then transferred and aligned on elastomer with tweezers. The bottom plate is placed on a thin elastomer film and the top plate is place over top while aligning the overlapping fingers of the two plates. A thin elastomer film is then placed on top of the sensor, sandwiching the two plates between elastomer films. Uncured elastomer is added around the sensor edges to seal the sensor. Both polydimethylsiloxane (PDMS; Sylgard 184, Dow Corning) and poly(styrene-isoprene-styrene) (SIS) were used as elastomer films. PDMS was used to attach elastomer layers together and seal the sensor. PDMS was mixed in a 10:1 ratio of base to curing agent. SIS solution was formed based on prior work, where 15 g of poly(styrene-isoprene-styrene) (14% styrene; Sigma-Aldrich) was mixed with 100 mL of propyl acetate (Alfa Aesar). For wired sensing of capacitive sensors, Cu wire was attached to the sensor using silver paint (Fast Drying Silver Paint; Ted Pella). For wireless sensing with a stent, silver paint was used to connect to the serpentine interconnections of the sensor to the two ends of the stent. The sensor is placed with the conductive side of the interconnect facing towards the stent and pressed together while the silver paint dries. PDMS was coated over the connections for insulation.

Microfabrication of wireless stent

A femtosecond laser (Optec) was used to fabricate the wireless stent from stainless steel tubing (Vita Needle, 304SS 14XX). First, the steel tubing is laser machined to remove material from the connector locations. The machined surfaces were electropolished and rinsed with DI water. PI was then coated onto the tubing and cured at 240 °C for 1 h. The coating process was repeated twice before sanding the tubing surfaces to remove PI. This allowed PI to only remain in the precut connector locations. Laser machining was performed to cut the remaining stent structure and followed by electropolishing and rinsing. An electroless gold plating solution (Sigma Aldrich) was used to surface plate the stent with approximately a 15 µm thick layer of Au. Electrodeposition was performed with a three-electrode system while temperature and pH of the solution were maintained at 55 °C and 8. PI may be added over the connector locations strengthen the filled PI connections. The plated stent was rinsed before insulating the stent with a 30 µm thick layer of parylene.

Characterization of strain sensor

Linear strain was applied to the sensors with a motorized test stand (Mark-10 ESM303) while capacitance was measured with an LCR meter (B&K Precision 891). The circumferential strain was applied by embedding sensors in silicone tubing and applying pressure within the tubing. The pressure was measured with a commercial sensor (Honeywell 26PCBFB6G). For strain sensor optimization tests, a linear strain of 4.8% was applied to all sensors. Cyclic stretching and cyclic bending were evaluated using the motorized test stand. Wireless signals from integrated stents and sensors were acquired using a loop antenna connected to a vector network analyzer (VNA; Tektronix TTR506A) to continuously monitor resonant frequency. Resonant frequency was recorded by locating the minimum in the S_{11} parameter.

Restenosis sensing in artery model

A coronary artery model was formed by molding silicone (Ecoflex 00–30, Smooth-On). The mold formed an artery with a 3 mm inner diameter, 2 mm thickness, and 100 mm length. Restenosis models included a restenosis of 60%, 75%, or 90% at the center of the artery model. To simulate blood viscosity and flow, a 58.5–41.5 mixture of water to glycerin was flowed through the artery model with a pulsatile pump (Harvard Apparatus). A flow rate of 60 mL min^{-1} at 60 b.p.m. was used to compare sensor signals at different levels of restenosis. The sensor and stent were embedded in the silicone artery model, which is consistent with typical tissue growth over implanted stents. Arterial strain was measured optically by recording videos of the artery during pulsatile flow. Each frame of the videos were converted to black and white images and the two edges of the artery were located. The change in artery diameter from the initial, zero flow diameter was measured in pixels from each frame. The amplitude of strain change was determined and normalized to normal artery models without restenosis. Strain changes were averaged over the location of the sensing area within the artery model. Wired and wireless signals from the sensor were acquired with the LCR meter and VNA, respectively. For restenosis detection, the amplitude of capacitance or resonance changes were compared at each restenosis case and normalized to the amplitude recorded in the normal artery.

Ex-vivo restenosis monitoring

Ovine hearts were collected for implantation of stents and sensors into the coronary arteries. A pulsatile pump was connected to the arteries via tubing to enable blood flow. Both a water and glycerin mixture and ovine blood was used for fluid flow in the coronary arteries. Restenosis was simulated by adding silicone (Ecoflex 00–20, Smooth-On) within the artery near the implanted sensor. An LCR meter and VNA were used to measure wired and wireless signals.

Hemocompatibility and biocompatibility tests

For hemocompatibility tests, citrated fresh ovine whole blood was distributed into a vacutainer tube where samples were placed for 2 h at 37 °C. Platelet deposition was quantified by lactate dehydrogenase assay. Biocompatibility was evaluated with rat vascular smooth muscles cells by an indirect contact method for 24 h. Cell viability was analyzed with MTS assay. Data was normalized to the negative control, which included cells cultured in cell medium only. Cell death was induced in the positive control with 1 M acrylamide dissolved in cell culture medium.

CRediT authorship contribution statement

Robert Herbert: Conceptualization, Investigation, Formal analysis, Writing. **Moataz Elsisy**: Investigation, Formal analysis. **Bruno Rigo**: Investigation, Formal analysis. **Hyo-Ryoung Lim**: Investigation, Formal analysis. **Hyeonseok Kim**: Investigation, Formal analysis. **Chanyeong Choi**: Investigation, Formal analysis. **Seungil Kim**: Investigation, Formal analysis. **Sang-Ho Ye**: Investigation, Formal analysis. **William R. Wagner**: Conceptualization, Resources, Funding acquisition. **Youngjae Chun**: Conceptualization, Supervision, Resources, Funding acquisition, Writing. **Woon-Hong Yeo**: Conceptualization, Supervision, Resources, Funding acquisition, Project administration, Writing.

Declaration of Competing Interest

The authors declare the following financial interests/personal relationships which may be considered as potential competing interests: Woon-Hong Yeo has patent pending to Georgia Institute of Technology.

Acknowledgments

We acknowledge the support of the National Institutes of Health (NIH R03EB028928). The content is solely the responsibility of the authors and does not necessarily represent the official views of the NIH. This work was also supported by the Georgia Tech Institute for Electronics and Nanotechnology Center for Human-Centric Interfaces and Engineering. Electronic devices in this work were fabricated at the Institute for Electronics and Nanotechnology, a member of the National Nanotechnology Coordinated Infrastructure, which is supported by the National Science Foundation (grant ECCS-2025462).

Appendix A. Supporting information

Supplementary data associated with this article can be found in the online version at doi:10.1016/j.nantod.2022.101557.

References

[1] P. Libby, J.E. Buring, L. Badimon, G.K. Hansson, J. Deanfield, M.S. Bittencourt, L. Tokgözoğlu, E.F. Lewis, Nat. Rev. Dis. Prim. 5 (2019) 1–18.
[2] N. Torres, M. Guevara-Cruz, L.A. Velázquez-Villegas, A.R. Tovar, Arch. Med. Res. 46 (2015) 408–426.
[3] Cardiovascular diseases (CVDsWorld Health Organization. ⟨https://www.who.int/en/news-room/fact-sheets/detail/cardiovascular-diseases-(cvds)⟩, 2021.
[4] M. Stuntz, A. Palak, Value Health 19 (2016) A641.
[5] A.P. Banning, A. Baumbach, D. Blackman, N. Curzen, S. Devadathan, D. Fraser, P. Ludman, M. Norell, D. Muir, J. Nolan, Heart 101 (2015) 1–13.
[6] F. Alfonso, R.A. Byrne, F. Rivero, A. Kastrati, J. Am. Coll. Cardiol. 63 (2014) 2659–2673.
[7] D. Buccheri, D. Piraino, G. Andolina, B. Cortese, J. Thorac. Dis. 8 (2016) E1150.
[8] S. Mohan, A. Dhall, Int. J. Angiol. 19 (2010) e66–e72.
[9] J.A. Ormiston, M.W. Webster, Am. Heart Assoc. (2016) e004249.
[10] L.H. Bonati, J. Gregson, J. Dobson, D.J. McCabe, P.J. Nederkoorn, H.B. van der Worp, G.J. de Borst, T. Richards, T. Cleveland, M.D. Müller, Lancet Neurol. 17 (2018) 587–596.
[11] B.K. Lal, K.W. Beach, G.S. Roubin, H.L. Lutsep, W.S. Moore, M.B. Malas, D. Chiu, N.R. Gonzales, J.L. Burke, M. Rinaldi, Lancet Neurol. 11 (2012) 755–763.
[12] D. Omeh, E. ShlofmitzRestenosis, StatPearls Publishing,, 2019.
[13] G.G. Stefanini, D.R. Holmes Jr., N. Engl. J. Med. 368 (2013) 254–265.
[14] N. Gonzalo, P.W. Serruys, T. Okamura, H.M. van Beusekom, H.M. Garcia-Garcia, G. van Soest, W. van der Giessen, E. Regar, Am. Heart J. 158 (2009) 284–293.
[15] K. Keikhosravy, A. Zargaran-Yazd, S. Mirabbasi, 2012, Annual International Conference of the IEEE Engineering in Medicine and Biology Society, IEEE2012, pp. 3231–3234.
[16] S. Cassese, R.A. Byrne, S. Schulz, P. Hoppman, J. Kreutzer, A. Feuchtenberger, T. Ibrahim, I. Ott, M. Fusaro, H. Schunkert, Eur. Heart J. 36 (2015) 94–99.
[17] M. Joner, A.V. Finn, A. Farb, E.K. Mont, F.D. Kolodgie, E. Ladich, R. Kutys, K. Skorija, H.K. Gold, R. Virmani, J. Am. Coll. Cardiol. 48 (2006) 193–202.
[18] R. Reejhsinghani, A.S. Lotfi, Vasc. Health Risk Manag. 11 (2015) 93.

[19] D.R. Holmes, D.J. Kereiakes, S. Garg, P.W. Serruys, G.J. Dehmer, S.G. Ellis, D.O. Williams, T. Kimura, D.J. Moliterno, J. Am. Coll. Cardiol. 56 (2010) 1357–1365.
[20] A. Kastrati, J. Mehilli, J. Dirschinger, J. Pache, K. Ulm, H. Schühlen, M. Seyfarth, C. Schmitt, R. Blasini, F.-J. Neumann, Am. J. Cardiol. 87 (2001) 34–39.
[21] R. Herbert, H.R. Lim, S. Park, J.H. Kim, W.H. Yeo, Adv. Healthc. Mater. 10 (17) (2021) 2100158.
[22] H.R. Lim, H.S. Kim, R. Qazi, Y.T. Kwon, J.W. Jeong, W.H. Yeo, Adv. Mater. 32 (2020) 1901924.
[23] R. Herbert, S. Mishra, H.R. Lim, H. Yoo, W.H. Yeo, Adv. Sci. 6 (2019) 1901034.
[24] Y.J. Hong, H. Jeong, K.W. Cho, N. Lu, D.H. Kim, Adv. Funct. Mater. 29 (2019) 1808247.
[25] C.M. Boutry, L. Beker, Y. Kaizawa, C. Vassos, H. Tran, A.C. Hinckley, R. Pfattner, S. Niu, J. Li, J. Claverie, Nat. Biomed. Eng. 3 (2019) 47–57.
[26] M.A. Fonseca, M.G. Allen, J. Kroh, J. White, Tech. Dig. Solid-State Sensor, Actuator, and Microsystems Workshop (Hilton Head 2006), Citeseer2006, pp. 37–42.
[27] J. Vishnu, G. Manivasagam, Med. Devices Sens. 3 (2020) e10116.
[28] X. Chen, B. Assadsangabi, Y. Hsiang, K. Takahata, Adv. Sci. 5 (2018) 1700560.
[29] D. Son, J. Lee, D.J. Lee, R. Ghaffari, S. Yun, S.J. Kim, J.E. Lee, H.R. Cho, S. Yoon, S. Yang, ACS Nano 9 (2015) 5937–5946.
[30] J. Park, J.-K. Kim, D.-S. Kim, A. Shanmugasundaram, S.A. Park, S. Kang, S.-H. Kim, M.H. Jeong, D.-W. Lee, Sens. Actuators B: Chem. 280 (2019) 201–209.
[31] M.N. Gulari, M. Ghannad-Rezaie, P. Novelli, N. Chronis, T.C. Marentis, 2014 IEEE 27th International Conference on Micro Electro Mechanical Systems (MEMS), IEEE 2014, pp. 893–896.
[32] M.N. Gulari, M. Ghannad-Rezaie, P. Novelli, N. Chronis, T.C. Marentis, J. Micro Syst. 24 (2014) 50–61.
[33] R. Lopez-Palop, E. Pinar, I. Lozano, D. Saura, F. Picó, M. Valdés, Eur. Heart J. 25 (2004) 2040–2047.
[34] P. Bingger, M. Zens, P. Woias, Biomed. Micro 14 (2012) 573–581.
[35] S.R. Ruth, M.-g Kim, H. Oda, Z. Wang, Y. Khan, J. Chang, P.M. Fox, Z. Bao, Iscience 24 (2021) 103079.
[36] D. Ruh, S. Subramanian, S. Sherman, J. Ruhhammer, M. Theodor, L. Dirk, K. Foerster, C. Heilmann, F. Beyersdorf, H. Zappe, Biomed. Opt. Express 7 (2016) 3230–3246.
[37] J.A. Chirinos, J. Cardiovasc. Transl. Res. 5 (2012) 243–255.
[38] N.A. Shirwany, M.-h Zou, Acta Pharmacologica, Sinica 31 (2010) 1267–1276.
[39] Y.S. Oh, Clin. Hypertens. 24 (2018) 1–3.
[40] M. Yambe, H. Tomiyama, Y. Hirayama, Z. Gulniza, Y. Takata, Y. Koji, K. Motobe, A. Yamashina, Hypertens. Res. 27 (2004) 625–631.
[41] M. Collette, A. Humeau, C. Chevalier, J.-F. Hamel, G. Leftheriotis, Hypertens. Res. 34 (2011) 578–583.
[42] N. Zavanelli, W.-H. Yeo, ACS Omega 6 (2021) 9344–9351.
[43] Q. Huang, Y. Zhu, Adv. Mater. Technol. 4 (2019) 1800546.
[44] Y. Khan, A. Thielens, S. Muin, J. Ting, C. Baumbauer, A.C. Arias, Adv. Mater. 32 (2020) 1905279.
[45] K.-S. Kwon, M.K. Rahman, T.H. Phung, S.D. Hoath, S. Jeong, J.S. Kim, Flex. Print. Electron. 5 (2020) 043003.
[46] P. Goel, J. Singh, J. Phys. D: Appl. Phys. 48 (2015) 445303.
[47] V. Tsouti, V. Mitrakos, P. Broutas, S. Chatzandroulis, IEEE Sens. J. 16 (2016) 3059–3067.
[48] S. Yao, Y. Zhu, Nanoscale 6 (2014) 2345–2352.
[49] D.J. Lipomi, M. Vosgueritchian, B.C. Tee, S.L. Hellstrom, J.A. Lee, C.H. Fox, Z. Bao, Nat. Nanotechnol. 6 (2011) 788–792.
[50] D.J. Cohen, D. Mitra, K. Peterson, M.M. Maharbiz, Nano Lett. 12 (2012) 1821–1825.
[51] L. Cai, L. Song, P. Luan, Q. Zhang, N. Zhang, Q. Gao, D. Zhao, X. Zhang, M. Tu, F. Yang, Sci. Rep. 3 (2013) 1–9.
[52] F. Xu, Y. Zhu, Adv. Mater. 24 (2012) 5117–5122.
[53] R. Nur, N. Matsuhisa, Z. Jiang, M.O.G. Nayeem, T. Yokota, T. Someya, Nano Lett. 18 (2018) 5610–5617.
[54] O. Atalay, Materials 11 (2018) 768.
[55] S.-R. Kim, J.-H. Kim, J.-W. Park, ACS Appl. Mater. Interfaces 9 (2017) 26407–26416.
[56] Y. Fan, Z. Shen, X. Zhou, Z. Dan, L. Zhou, W. Ren, T. Tang, S. Bao, C. Nan, Y. Shen, Adv. Mater. Technol. (2021) 2101190.
[57] J. Shintake, T. Nagai, K. Ogishima, Front. Robot. AI 6 (2019) 127.
[58] C.M. Boutry, Y. Kaizawa, B.C. Schroeder, A. Chortos, A. Legrand, Z. Wang, J. Chang, P. Fox, Z. Bao, Nat. Electron. 1 (2018) 314–321.
[59] T. Numao, K. Ogawa, H. Fujinuma, N. Furuya, J. Cardiol. 30 (1997) 1–8.
[60] M. Back, G. Kopchok, M. Mueller, D. Cavaye, C. Donayre, R.A. White, J. Vasc. Surg. 19 (1994) 905–911.
[61] S. Nakatani, M. Yamagishi, J. Tamai, Y. Goto, T. Umeno, A. Kawaguchi, C. Yutani, K. Miyatake, Circulation 91 (1995) 2904–2910.
[62] J.T. Dodge Jr, B.G. Brown, E.L. Bolson, H.T. Dodge, Circulation 86 (1992) 232–246.
[63] J. Kim, M. Kim, M.-S. Lee, K. Kim, S. Ji, Y.-T. Kim, J. Park, K. Na, K.-H. Bae, H. Kyun, Kim., Nat. Commun. 8 (2017) 1–8.
[64] W.-J. Deng, L.-F. Wang, L. Dong, Q.-A. Huang, IEEE Sens. J. 18 (2018) 4886–4892.
[65] G. Biglino, P. Verschueren, R. Zegels, A.M. Taylor, S. Schievano, J. Cardiovasc. Magn. Reson. 15 (2013) 1–7.
[66] M. Stevanov, J. Baruthio, B. Eclancher, J. Appl. Physiol. 88 (2000) 1291–1294.
[67] A. Benbrahim, J. Gilbert, B.B. Milinazzo, D.F. Warnock, S. Dhara, J.P. Gertler, R.W. Orkin, W.M. Abbott, J. Vasc. Surg. 20 (1994) 184–194.
[68] M. Elsisy, R. Herbert, W.-H. Yeo, J.J. Pacella, Y. Chun, Nano-, Bio-, Info-Tech Sensors and Wearable Systems, Int. Soc. Opt. Photonics (2021) 1159006.
[69] A.R. Mohammadi, K. Chen, M.S.M. Ali, K. Takahata, Biosens. Bioelectron. 30 (2011) 300–305.
[70] C. Balan, C. Balut, L. Gheorghe, C. Gheorghe, E. Gheorghiu, G. Ursu, Clin. Hemorheol. Micro 30 (2004) 359–364.
[71] A. Peyman, C. Gabriel, E. Grant, Bioelectromagnetics: Journal of the Bioelectromagnetics Society, The Society for Physical Regulation in Biology and Medicine, Eur. Bioelectromagn. Assoc. 28 (2007) 264–274.
[72] X. Chen, D. Brox, B. Assadsangabi, Y. Hsiang, K. Takahata, Biomed. Micro 16 (2014) 745–759.
[73] D. Hukins, A. Mahomed, S. Kukureka, Med. Eng. Phys. 30 (2008) 1270–1274.
[74] J.T. Reeder, J. Choi, Y. Xue, P. Gutruf, J. Hanson, M. Liu, T. Ray, A.J. Bandodkar, R. Avila, W. Xia, Sci. Adv. 5 (2019) eaau6356.
[75] C.J. Bettinger, M. Ecker, T.D.Y. Kozai, G.G. Malliaras, E. Meng, W. Voit, MRS Bull. 45 (2020) 655–668.
[76] X. Xie, L. Rieth, S. Merugu, P. Tathireddy, F. Solzbacher, Appl. Phys. Lett. 101 (2012) 093702.
[77] E. Song, R. Li, X. Jin, H. Du, Y. Huang, J. Zhang, Y. Xia, H. Fang, Y.K. Lee, K.J. Yu, ACS Nano 12 (2018) 10317–10326.
[78] E. Song, J. Li, J.A. Rogers, APL Mater. 7 (2019) 050902.
[79] C. Li, M. Cauwe, Y. Yang, D. Schaubroeck, L. Mader, M. Op de Beeck, Coatings 9 (2019) 579.